UNCONVENTIONAL RESOURCES TECHNOLOGY CONFERENCE
FUELED BY SPE • AAPG • SEG

URTeC: 2154184

Integrating 3D Seismic and Geomechanical Properties with Microseismic Acquisition and Fracturing Parameters to Optimize Completion Practices within the Wolfcamp Shale Play of the Midland Basin

Michael Shoemaker*[1], Nancy Zakhour[2], and Joshua Peacock[1]
1. Callon Petroleum Company, Houston, Texas, United States. 2. Schlumberger, Houston, Texas, Unites States

Summary

This study presents a successful empirical approach based on the integration of numerous multidisciplinary measurements to optimize completion methodologies and future field development strategies for stacked lateral wellbores, and essentially to high-grade exploratory Wolfcamp landing zones from 3D seismic data. Specifically, we measured mineralogical and geomechanical shale properties directly from 3D surface seismic data lengthwise along lateral well trajectories at individual frac stages which were monitored real-time using microseismic acquisition. Linear regression analyses for calibration show strong correlations between inverted seismic P-wave impedance versus microseismic data and fracture pressure responses, shale mineralogy compositions, and geomechanical properties calculated from core data.

The method was recently tested in the prolific oil-bearing Wolfcamp shale-oil play of the Midland Basin, West Texas, on three horizontal laterals drilled in a “chevron pattern”, two of which in the deeper Wolfcamp B formation and the third in the Wolfcamp A. Real-time microseismic monitoring was used to observe the hydraulic fracturing treatments and the resulting heights and lateral extent. Although identical pumping schedules were initially intended for all three laterals stimulated in a “zipper sequence”, with geometric stage placement, it became apparent during the treatments that microseismic height growth varied significantly across the given laterals within individual stages.

The results of our combined analysis showed that microseismic fracture height variability is most influenced by changes in shale stratigraphy and subsequent mineralogy composition, without a definitive relationship with treatment injection rates. Optimal fracture heights were observed in landing areas with significant volume of calcite, characteristic of high Young’s modulus and closure stress, variables which in turn were estimated from 3D seismic. For validation, production history of said laterals and numerous others in the field confirms a strong correlation between seismic P-wave impedance and initial 120 day cumulative oil in landing zones where high volume of calcite and hence brittleness exists.

Introduction

The prolific Wolfcamp (shale) formation is a tight oil play of the greater Permian Basin hydrocarbon province located in West Texas (Fig. 1a) which has seen, in just a few short years, a steep increase in horizontal drilling activity within low permeable reservoirs that are estimated to contain recoverable reserves greater than 50 billion BOE. What is particularly unique about the Wolfcamp when compared to other North American shale oil plays is its thickness which can exceed in upwards of 2,500’ in places, thus allowing for multiple zones of stacked pay. This translates to millions of additional acres of potential horizontal development when defined in 3D space.

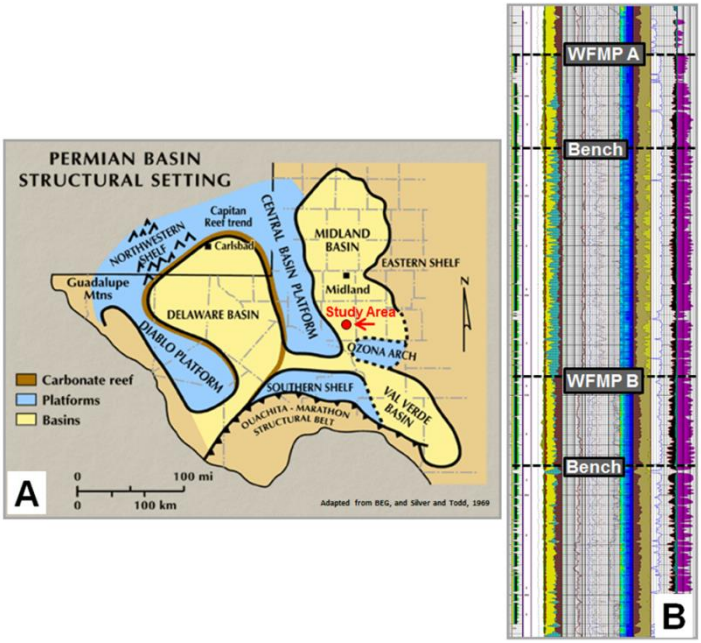

Figure 1: A) Paleostructure map of the Permian Basin. B) Petrophysical type well Neal 307 showing mineralogy of the Wolfcamp A & B.

Lateral wells are typically 7,500 to 8,000' length wise with some operators drilling and completing stacked horizontals from multi-well pads in "chevron-type patterns" (Fig 2a.) for improved economics resulting from lower drilling and completion costs. Higher IP rates are also being achieved by simultaneously completing and fracking multiple wells in a "zipper sequence" which increases hydraulic fracture stimulation efficiency. Said production increases are particularly critical in low cost environments during times of low crude oil prices.

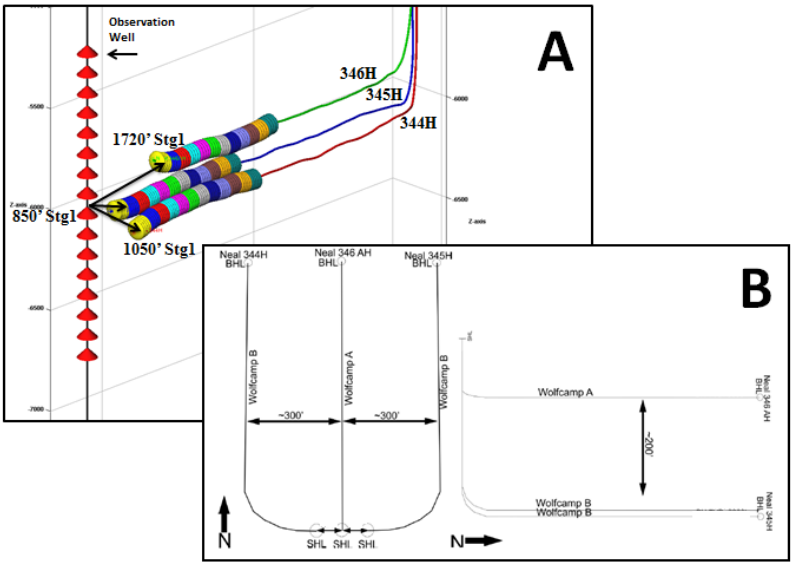

Figure 2: A) Stacked lateral wells in a "chevron pattern". B) Well spacing targeting the Wolfcamp A and B.

Operators in the southern Midland Basin (Fig. 1a), which is central to current horizontal development, have designated the Wolfcamp formation into four independent landing zones or subsections termed the A, B, C, and D (or Cline) with each zone well within the oil window, and containing varying volumes of mineral compositions including quartz, limestone, clay, and kerogen. Microseismic data was only acquired for the Wolfcamp A and B zones, and therefore will be the focus of this paper.

The Wolfcamp B (Fig. 1b) typically results in relatively higher IP rates and greater EUR's, and is perhaps considered the "lower hanging fruit" of the four zones due to ideal mineralogy for enhanced brittleness and greater oil saturations, followed by the Wolfcamp A which typically contains massive carbonate detrital deposits toward its base which can act as frac barriers. The C and D zones are deeper in section and hence have higher fracture gradients, and are increasingly influenced by deeper seated structures that can potentially induce geosteering challenges. For all zones however, the assemblage of mineralogy compositions define mechanical layers that are most prone to fracturing, which is a function of lateral and vertical depositional (or mineralogical) facies changes. Examples of Wolfcamp mineralogy variability basin wide is shown in Figure 3. Volumes were estimated from petrophysical logs acquired in vertical wellbores from central to southern areas of the Midland Basin. Values represent averages calculated from the Wolfcamp A and B flooding surface and bench (defined below).

The first objective of this paper is to define basin mineralogy of the Wolfcamp A and B intervals, and its influence in defining geomechanics and fracability, followed by the estimation of such properties from surface seismic data. Next, the seismic interpretation and integration process will be discussed, which will then lead into the microseismic data acquisition and engineering completions analysis with implications for fracture modeling, prop height and half-length simulation followed lastly by seismic interpretation examples. For all sections, analysis will focus on the 345H which was the first of the two horizontal Wolfcamp B wells to be fracture stimulated in the zipper sequence.

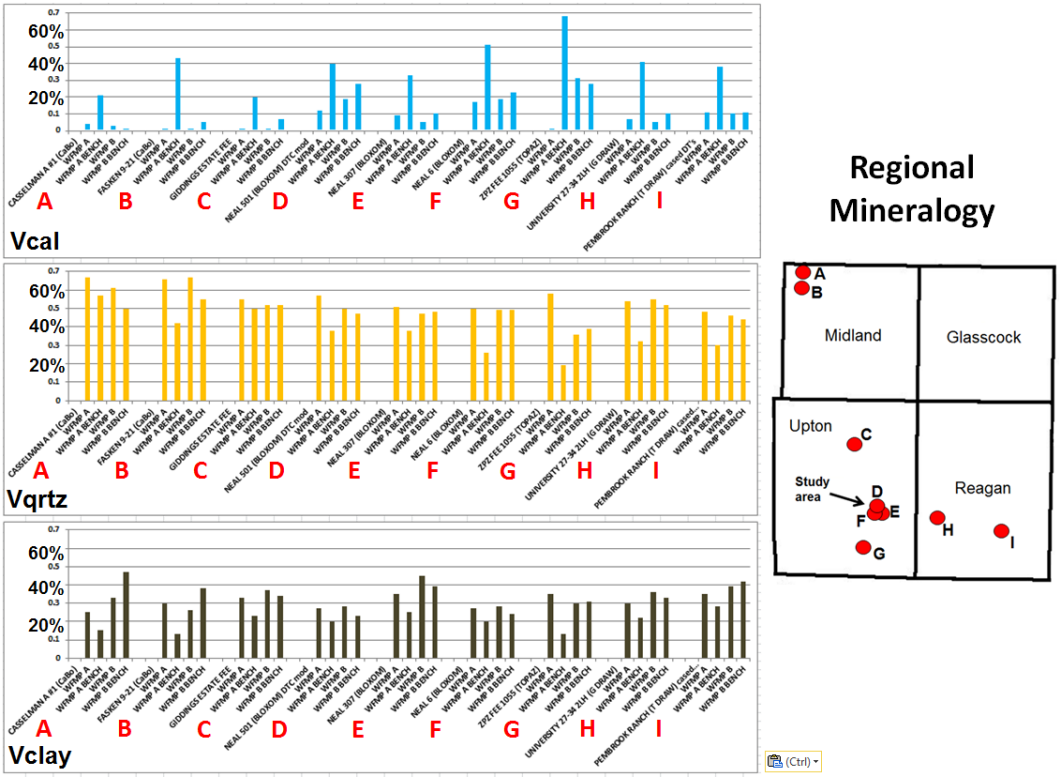

Figure 3: Mineralogy compositions for the Wolfcamp A and B flooding surface and bench, basin wide. Neal 307 is well E.

Wolfcamp Shale Mineralogy of the Midland Basin

Geologically, Wolfcamp rocks of the central and southern Midland Basin are characteristic of kerogen-rich dark shales and interbedded detrital carbonates, muds, and sands that were deposited predominately by debris / gravity flows and turbidity currents down slope from the Central Basin Platform or CBP (Wilson, 1975), and likely were deposited in a proximal basin plain environment. Shelf-ward toward the CBP, carbonate deposition increases to a point where large detached blocks of dolostone are common proximal to the platform margin (Mazzullo and Reid, 1987). Therefore, abundance and distribution of carbonate-rich detrital flows can be used as a proxy in determining relative distances from the CBP margin which in turn defines carbonate fairways more prone to fracture stimulation for increased production when high grading acreage for development.

Each Wolfcamp zone can be further subdivided into two units (Fig. 1b.): a high volume of clay ductile "flooding surface" interval which saw minimal carbonate shedding, and a more brittle calcite-rich carbonate "bench" interval. The flooding surface and bench intervals were deposited in sea-level highstand and lowstand systems tracts, respectively. Operators typically land lateral wellbores below the flooding surface and within the more brittle carbonate bench in hopes of optimal hydraulic fracture initiation of wide fracture networks nearest the wellbore. This allows for fracture propagation and proppant embedment into the relatively ductile (A and B) flooding surface above, which typically contains a greater volume of kerogen and oil saturation.

Unlike the relatively ductile flooding surface, the carbonate bench is more fracture prone with a higher volume of calcite (shed down slope from the CBP), which strongly correlates to dynamic Young's Modulus (YM) shown in Figure 7b which represents a geomechanical characterization of tensile strength or stiffness, and defines the ratio of stress to strain, or the rock's ability to maintain a fracture. Poisson's Ratio (PR) is also a rock mechanical property, and is defined as the ratio of lateral strain to longitudinal strain which quantifies the rock's ability to fail under stress. When combined, these two variables define the rock's fracability expressed as a brittleness index (Rickman, et. al., 2008) which was calculated herein using the p-sonic and dipole logs from the Neal 307 (Fig. 1b). A correlation of the brittleness index verses Vclay is shown in Figure 7a which shows brittleness decreasing as calcite is subtracted-out and replaced by greater volume of clay, thus increasing ductility and the rock's inability to prop up fractures. A general rule of thumb in shale plays says the lower the PR and higher the YM, the more brittle and fracture competent the rock likely is.

Wolfcamp geomechanical properties representing identical zones defined in Figure 3 are shown in Figure 4 for the same wells. Again, values represent zone averages. Notice per zone, volume of calcite (Vcal) and YM increasing proportionally in most cases due to decreasing volume of clay (Vclay). YM values representing the

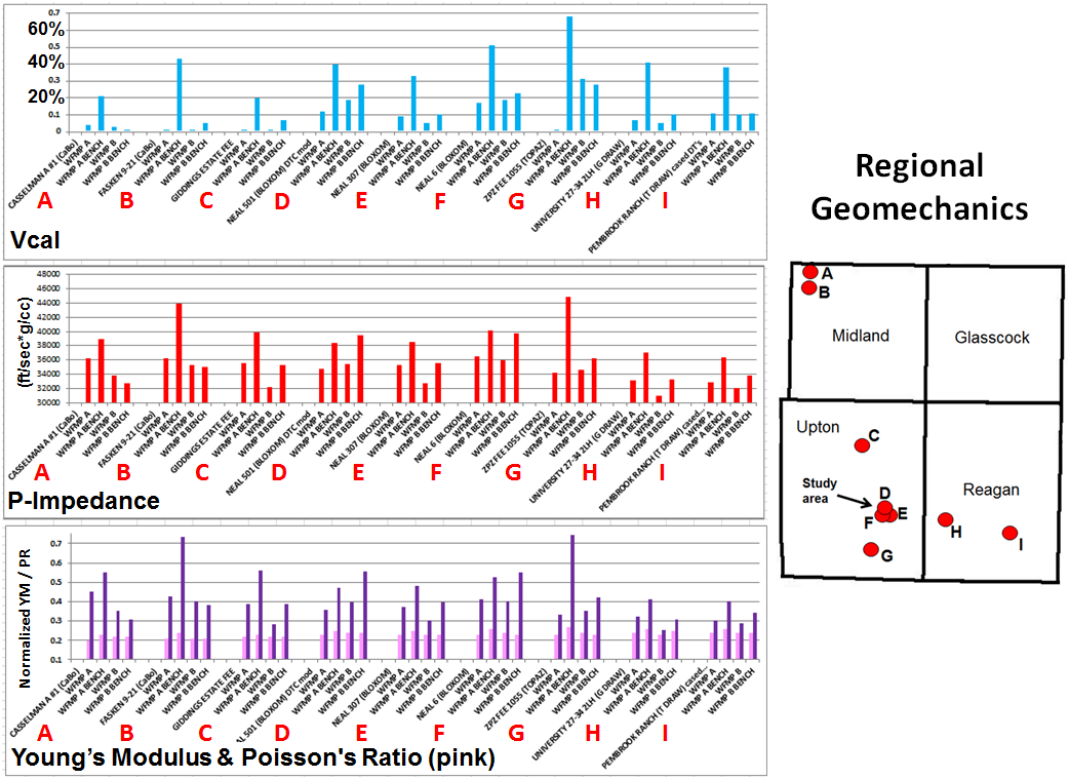

Figure 4: Geomechanics for the Wolfcamp A and B flooding surface and bench, basin wide. Neal 307 is well E.

bench and flooding surface vary significantly from 30-75 GPa to 25-40 GPa, respectively. Although quartz is a more brittle substance and most prone to fracturing, it's variability throughout the basin is minimal, and similar to PR which also shows minimal variability and ranges only from 0.21 to 0.24 (Fig. 4). Therefore, PR is not likely an ideal

proxy for characterizing brittleness in the Wolfcamp. However, crossplots in Figure 6 confirm strong correlations and linearity between Vclay and YM basin wide, in addition to acoustic p-impedance (P-imp). Specifically, as Vclay decreases and is replaced by Vcal, YM increases linearly with increasing values of P-imp which is a rock property measurement that can be estimated directly from inverted 3D surface seismic data.

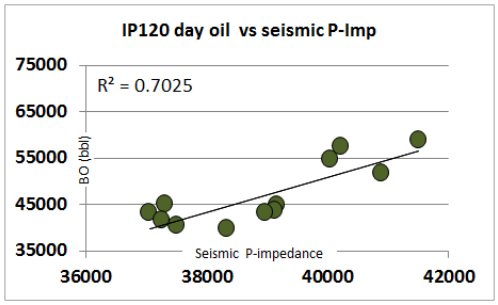

Figure 5: A good correlation exists between seismic p-imp and initial 120 day BO cumulative production from adjacent laterals.

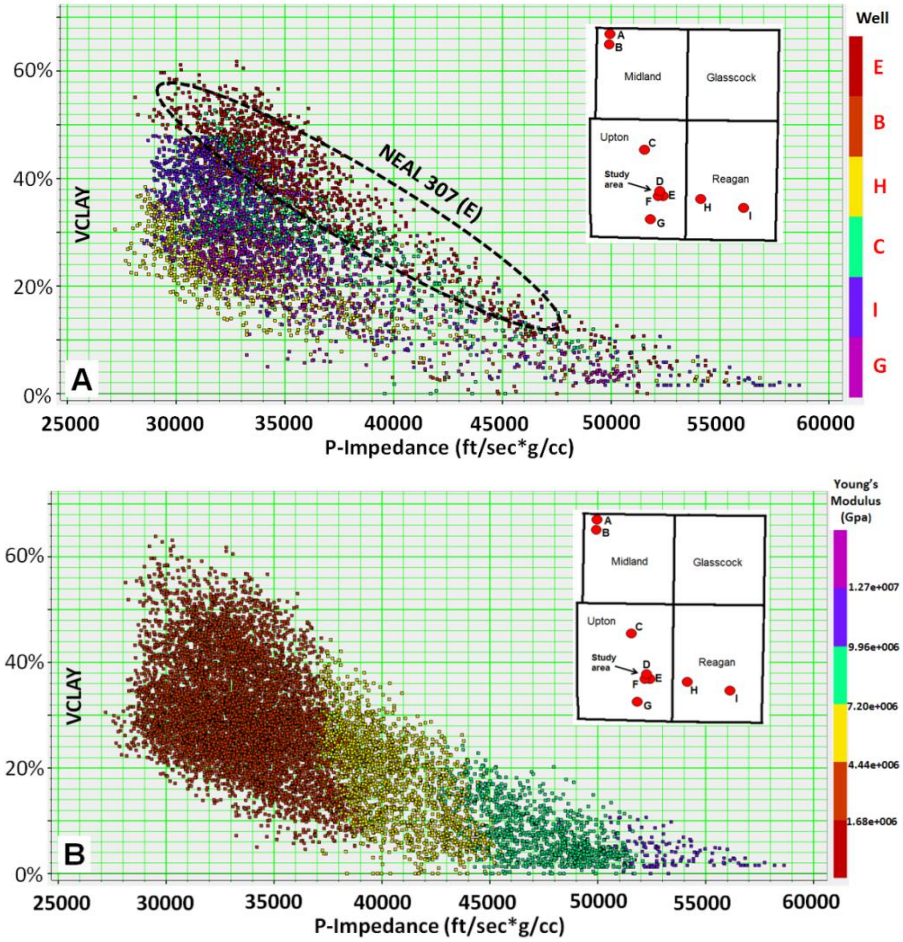

Figure 6: Regional well crossplots showing correlations of p-impedance with A) B Bench Vclay only and B) Young's Modulus (color) for all Wolfcamp A and B zones.

Figure 5 shows the correlation between initial 120 day cumulative oil production of adjacent lateral wells in the field with average p-impedance extrapolated length wise along each of the well trajectories. Higher producing wells correlate to higher magnitudes of p-impedance where Vcal is interpreted to exist and characterized by higher values of brittleness, likely resulting from more efficient fracture stimulation and greater production rates. Better producing

wells are located in the extreme northwest quadrant of the field (see Fig. 7 maps) where a carbonate-rich (detrital) lobe has been interpreted and confirmed by vertical wellbore petrophysical logs.

Therefore, a high degree of vertical and lateral heterogeneity exists within the Wolfcamp formation that is geology driven, and results from the irregular stacking of discrete depositional carbonate units (Hobson and others, 1985) resulting in varying mineralogy compositions that ultimately define and correlate with geomechanical properties characterized by relative fracability and brittleness. These mechanical properties ultimately influence resultant fracture stimulation geometries including hydraulic fracture height and half-length which in turn require calibration to microseismic and completions data. This empirical approach demonstrates the integration of said multidisciplinary measurements to optimize completion parameters with lower costs using stage by stage analysis, and to improve fracture modeling workflows for a more complete and accurate solution for optimal production rates.

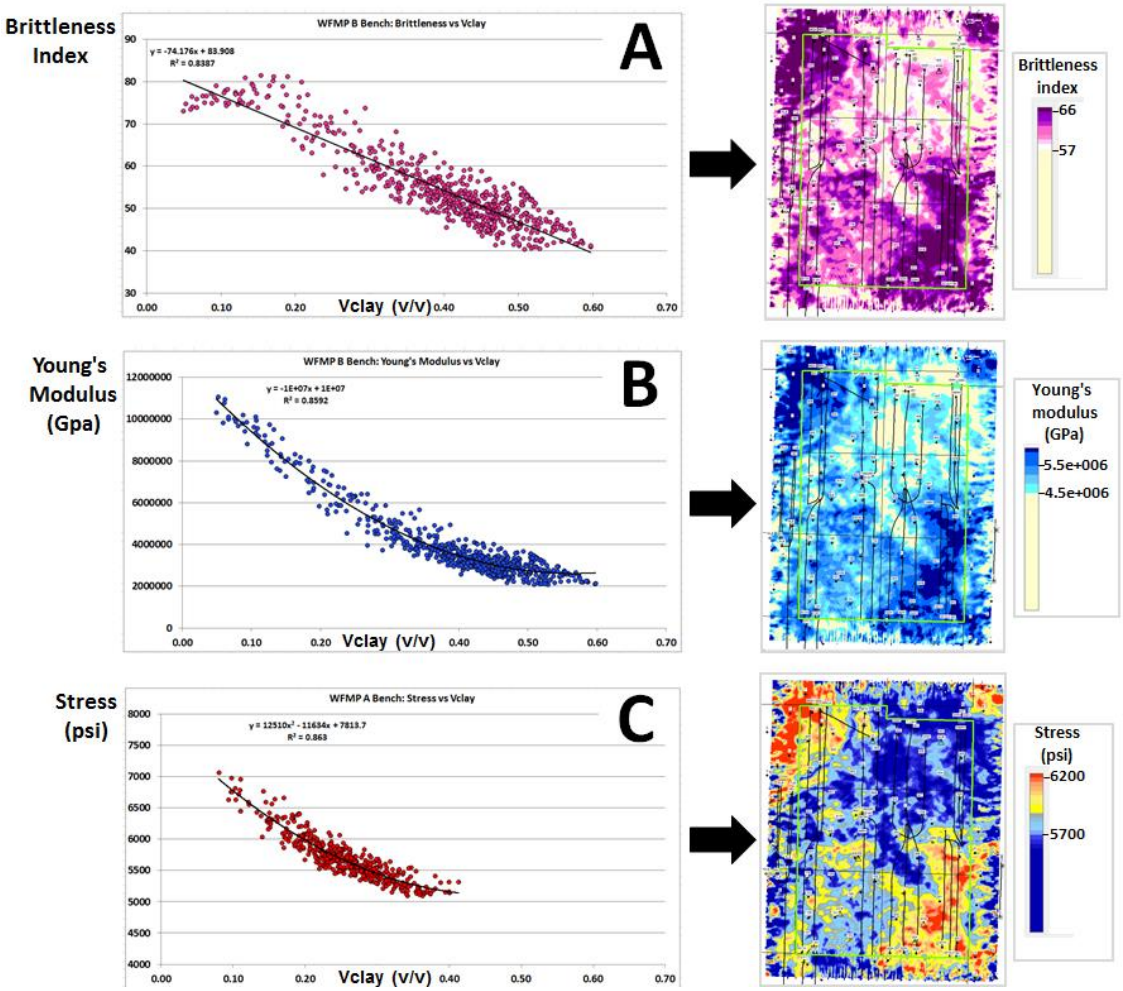

Figure 7: Zone wise crossplots showing strong correlations between Vclay and geomechanical properties including: A) Brittleness index, B) Young's modulus, and C) Stress. Geomechanical data points originating from dipole and p-sonic logs representing the Neal 307 (Fig. 1b) were taken from the top to base Wolfcamp B bench only. Resulting maps were ultimately used to extrapolate seismic pseudo lateral logs defined in Figure 8.

3D Surface Seismic Inverted Impedance and Integration

The normal incidence poststack 3D surface seismic data was acquired with 82.5' bin spacing, and was processed to preserve relative amplitude and for zero phase. The data was inverted to p-impedance resulting in rock property units of (ft/sec*g/cc) to allow for the integration and correlation of surface seismic data with petrophysical and geomechanical dipole logs and microseismic data. The seismic inversion process (Saroka and Shoemaker, 2003)

included deterministic wavelet estimation to ensure zero phase data resulting in peak energy seismic response at acoustic interfaces for the extrapolation of accurate p-impedance maps. Mixed or rotated phase data would result in varying energy distributions across seismic amplitude events, resulting in erroneous results (Shoemaker, 2006) not characteristic of true stratigraphic and mineralogical variability. Due to high volume of calcite, seismic response to bench horizons represents a peak (or high p-impedance), converse to flooding surfaces which are clay-rich and are represented by low impedance troughs. Relative thickness of the Wolfcamp A and B bench and flooding surface are well within the resolvable limits of the seismic data, as is lateral resolution (Fresnel-zone) which was essential when extrapolating pseudo lateral logs from the seismic. The utility of prestack simultaneous inversion was investigated, however due to the minimal size of the seismic survey the required long offsets were not available

To capture local lateral variability of rock properties, zone wise cross plots from the Neal 307 (Fig. 1b), representing the Wolfcamp A and B bench of log p-impedance vs. Vclay, Vcal, Young's Modulus and closure stress, show strong correlations, resulting in linear transform functions which were then used to create mineralogical and geomechanical seismic volumes of each property. Zone wise attribute maps representing said correlations were then created which enabled the direct extrapolation of such properties length wise along the wellbores in creating seismic pseudo lateral logs defined below. Figure 7 shows specific correlations of Vclay vs Young's modulus, closure stress and brittleness index; the linearity of which confirms that the Vcal replacement of Vclay results in greater stimulation fracability.

The workflow example in Figure 8 shows the end result of an extrapolated pseudo Vclay log followed by a full suite of logs which were then reformatted to a LAS file (Fig. 9) to allow for input into completions and fracture modeling software. Now, surface seismic rock properties nearest the lateral wellbore, where microseismic and completions data were acquired can be modelled, versus data interpolated potentially at significant distances from the study area. A more detailed and unique stage by stage analysis using the surface seismic impedance can now be integrated with completions and microseismic data, and fracture models for a more "smart frac" analysis in determining optimal fracture stimulation and completion parameters for future wells. Figures 24 to 30 show examples of the inverted seismic impedance integrated with microseismic data.

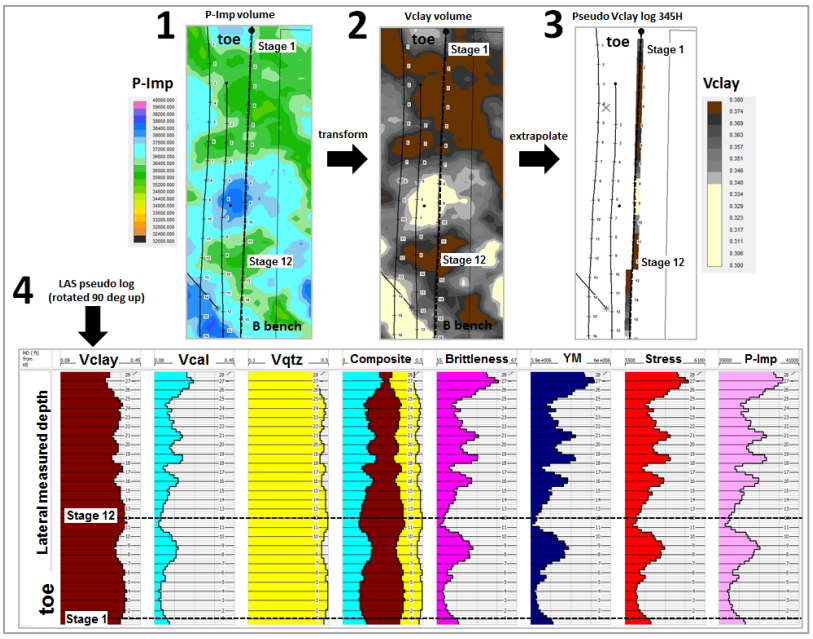

Figure 8: Workflow showing the extrapolation of seismic pseudo lateral logs from 3D surface seismic data. Example shown is for the 345H lateral well. Maps representing geomechanical properties are shown in Figure 7. The workflow was repeated for the 344H and 346AH wells.

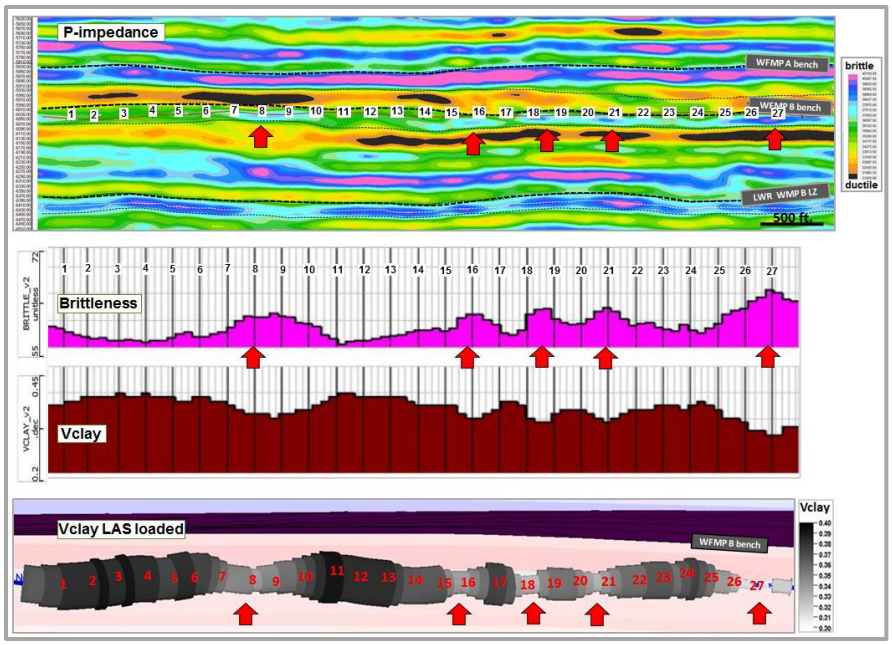

Figure 9: Top panel shows an arbitrary inverted p-impedance cross section length wise along the 345H lateral well. The middle panel shows the resulting brittleness and Vclay pseudo lateral logs extrapolated using the workflow defined in Figure 8. The bottom panel shows the pseudo Vclay log that has been LAS formatted, and then loaded into discrete fracture network modeling software for a more accurate measurement of the lateral mineralogical heterogeneity. Red arrows identify particular stages that are calcite-rich and thus more brittle.

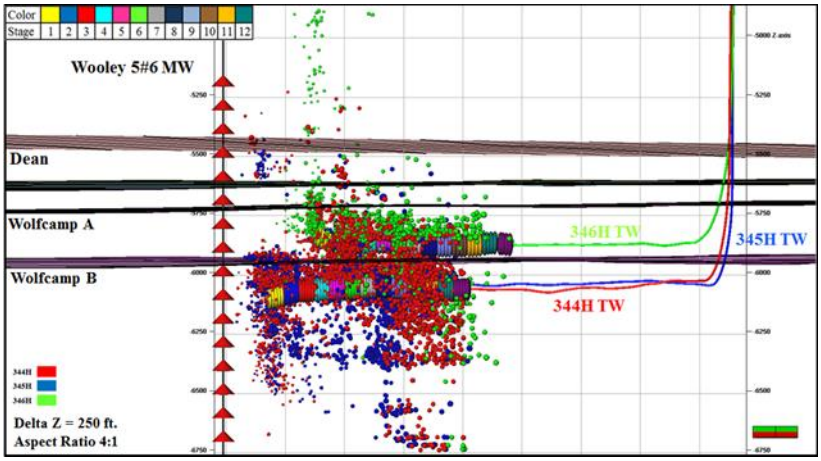

Figure 10: Depth view of the microseismic activity of each of the 3 laterals landed in the Wolfcamp A and B formations; Microseismic events are colored by well and sized by magnitude. Treatment and monitor wells are labeled on the plot by TW and MW respectively.

Microseismic Interpretation and Integration

Three laterals were completed in a chevron pattern (Fig. 2a) with simultaneous zipper fracturing. The Neal 346AH landed in the Wolfcamp A bench, and was treated first, followed by the Neal 345H and Neal 344H wells which were landed in the Wolfcamp B bench. An identical hydraulic fracturing treatment pump schedule was designed for all three laterals. The pump schedule consisted of slickwater fluid with 100 mesh sand and 40/70 white sand. The laterals were also completed using geometrical completion spacing.

Microseismic acquisition was used in real-time to assist with treatment parameter adjustment to essentially control excessive height growth (Zakhour et al., 2015). The main concern was the completion of stages 4 and onwards

toward the heel of the wells, particularly the deeper Wolfcamp B wells as they happen to be aligned with the shallower Wolfcamp A stages which would potentially lead to interference between the fractures developed. The first 12 toe-ward stages of each of the laterals were monitored using a 16-receiver downhole array deployed at one position in the vertical section of the monitor well (MW), the Wooley 5 #6. Stages beyond stage 12 were not monitored due to increasing distance and longer offsets from the receiver array.

Given the consistency in the stimulation and completion design with almost no variability encountered with the treatment implementation, the microseismic distribution with the hydraulic fracture geometry were expected to be relatively consistent from one stage to the other in each lateral. However, the observed microcosmic data suggests that the stages treated very differently. Figure 10 presents a depth view image of the microseismic activity seen on each of the treatment wells with the events colored by well.

Throughout the real-time fracturing operations, treatment slurry rate adjustments were made to limit the upward microseismic height growth observed on some of the stages. Figures 11 and 12 show the average rates per stage along with the correlations between the treatment slurry rates and the observed microseismic event depths respectively. It appears that despite the real-time variations in stimulation treatment rates to control the observed microseismic height development, the microseismic distribution did not display consistent behavior with the implemented changes.

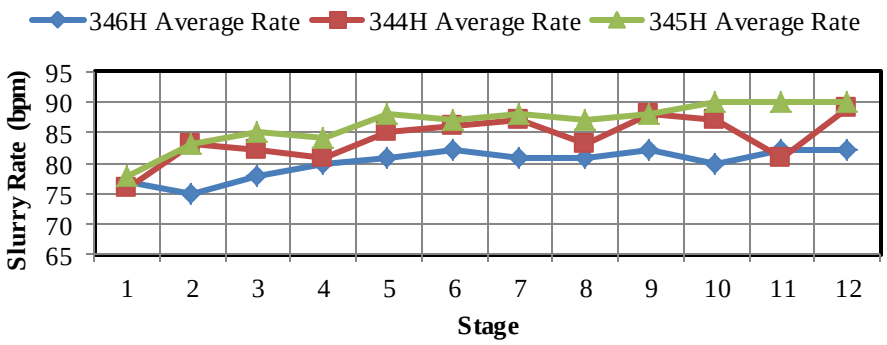

Figure 11: Average treatment slurry rate per stage for each of the 346H, 344H and 345H laterals

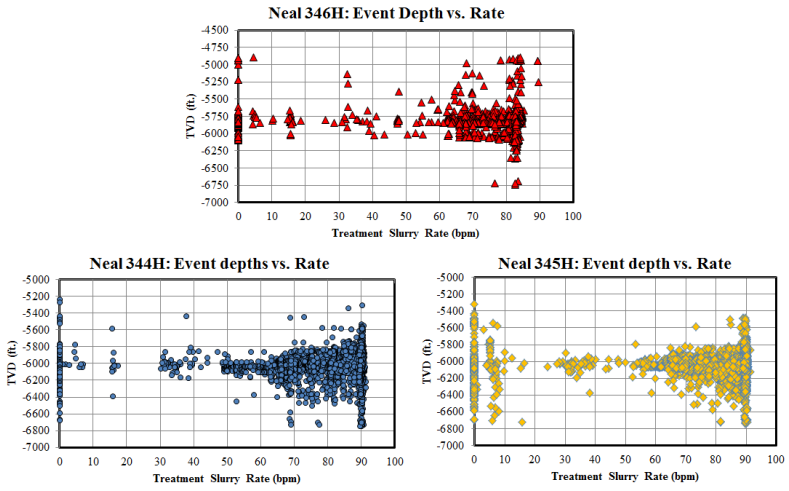

Figure 12: Microseismic event depth vs. treatment rate for each of the 346H, 344H and 345H laterals

To further investigate the observed microseismic variation, vertical log measurements were analyzed. The microseismic distribution from the Neal 345H is used to evaluate the variation in developed fracture geometry, primarily height growth. Geomechanical and petrophysical log measurements from an offset pilot hole well, the Neal 307 (Fig. 1b) located less than ~0.5 miles away, are presented alongside the Neal 345H microseismic events displayed in depth for stages 1 through 12 in Figure 13. Here the variation in height growth can be clearly identified.

It appears that the upper boundary that would potentially be limiting upward fracture height growth and microseismic activity is variable from one segment of the lateral to the next. The downward growth appears to show a more consistent change as more stages are completed with an increase in overall microseismic downward growth with the stages toward the heel.

Without a clear understanding of the lateral changes in rock properties at different depths, it becomes more challenging to determine the variations in fracture treatment pressure responses, in addition to microseismic event distribution and source parameter (Yu et al., 2014). Using vertical logs from the Neal 307, potential fracture barriers could be identified. The minimum in-situ stress is respectively propagated across a 3D geomechanical grid that takes into account the stratigraphic framework from 3D seismic which is shown in Figures 14 and 15.

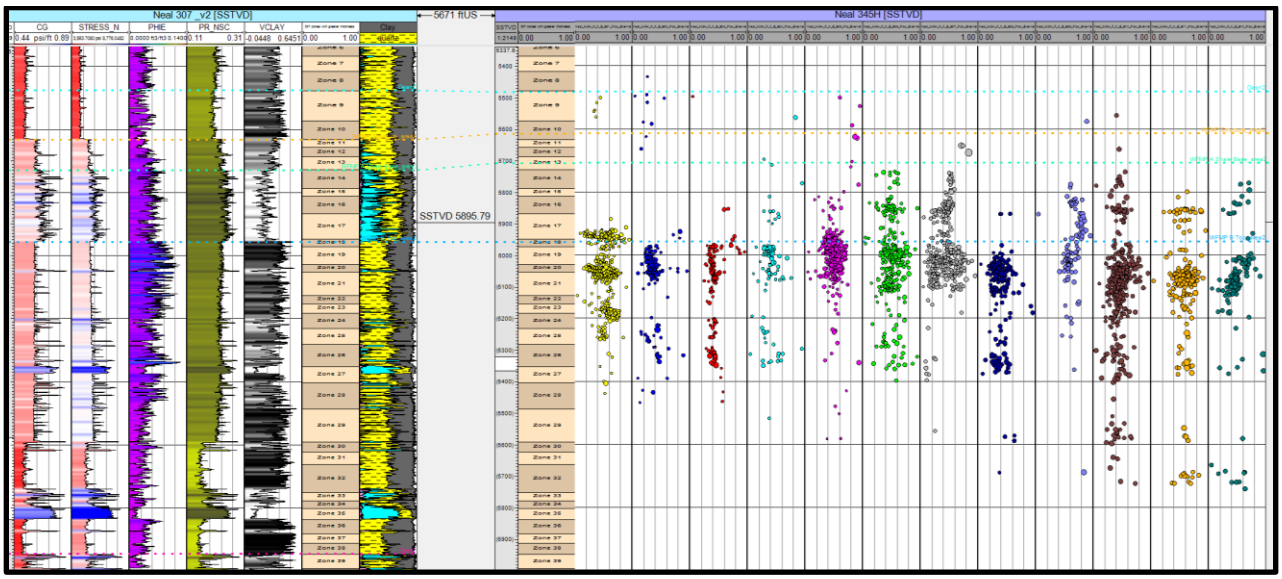

Figure 13: Neal 307 Pilot Hole Log (petrophysical and geomechanical properties) displayed against the microseismic event distribution from the Neal 345H; Events are colored by stages and displayed in chronological order from left to right

As numerous fracture barriers could be identified by examining the contrast from low to high stress regions, the microseismic height growth distribution remains inconclusive. The zone wise consistent laterally interpolated stress profile appears to be matching the microseismic height on only a few stages, and therefore fails to capture the lateral facies variability that can influence microseismic fracture response as defined above.

Based on event location, the majority of the event densities locate within the lower stress zones of the Wolfcamp B formation. However, when examining the event magnitudes and seismic moments, it appears that the upward and downward distribution of microseismic events is contributed by those of larger magnitudes and seismic moments. The depth view image herein, presents a cumulative moment release map where the seismic moments of all events within a 50' cell size are summed to provide a cumulative moment within that cell. All moments of values less than 4e+6 N.M. are filtered out to exaggerate the contribution of the larger seismic moments. It appears that some of the shallower and deeper microseismic events within the higher stress zones still maintain a significant presence post filtering, consequently emphasizing their contribution to the overall microseismic height growth seen.

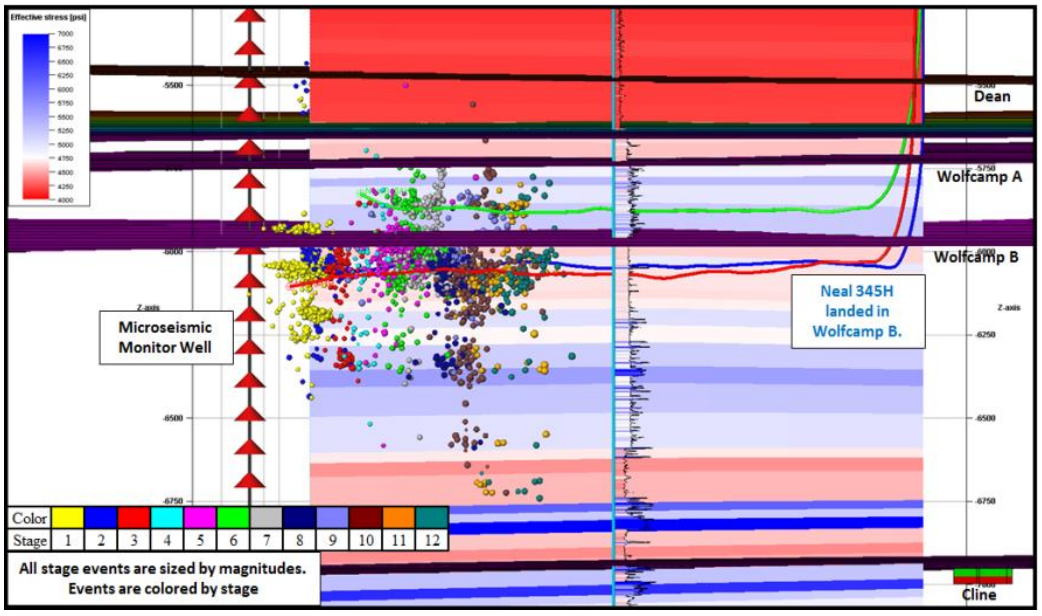

Figure 14: Neal 345H microseismic events per stage displayed against a zoned stress profile

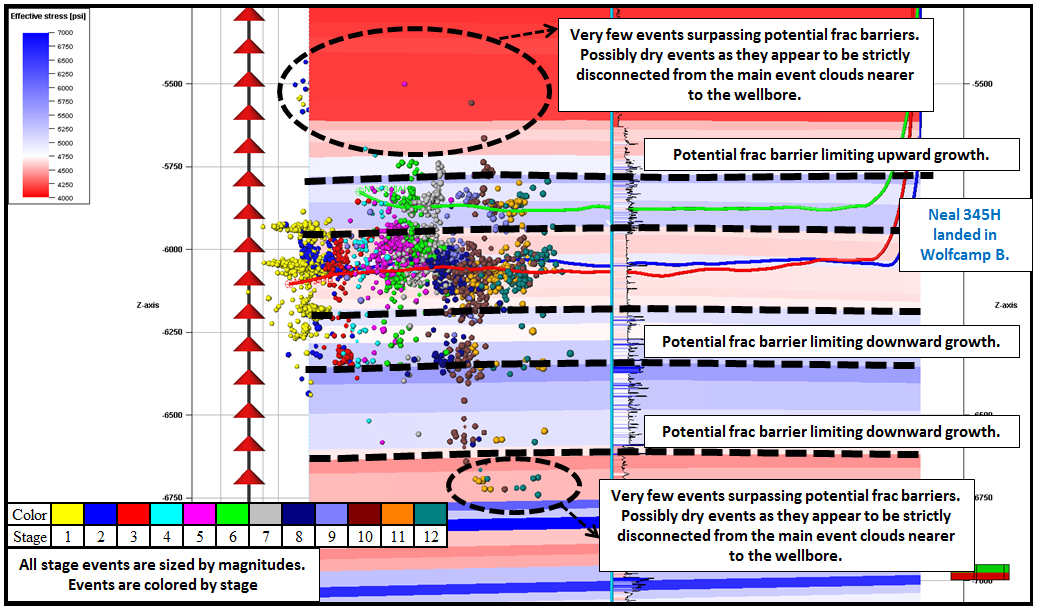

Figure 15: Neal 345H microseismic events per stage displayed against a zoned stress profile

A closer look at stages 5 and 10 of the Neal 345H is evaluated (Figures 17 and 18). Stage 5 stimulation of the Neal 345H indicates that the majority of the microseismic activity develops with an upward height growth where most of the event density locates within the lower stress zones of the Wolfcamp B formation (above the wellbore). Few events do propagate shallower into the Wolfcamp A where the 346H lateral is located and more dispersed events are scattered within deeper portions of the Wolfcamp B in lower and higher stress zones. It is clear that stage 5 sees a relatively decent height confinement compared to the microseismic distribution on the remaining stages of the 345H lateral (also see Figures 24, 25, and 26, stage 5).

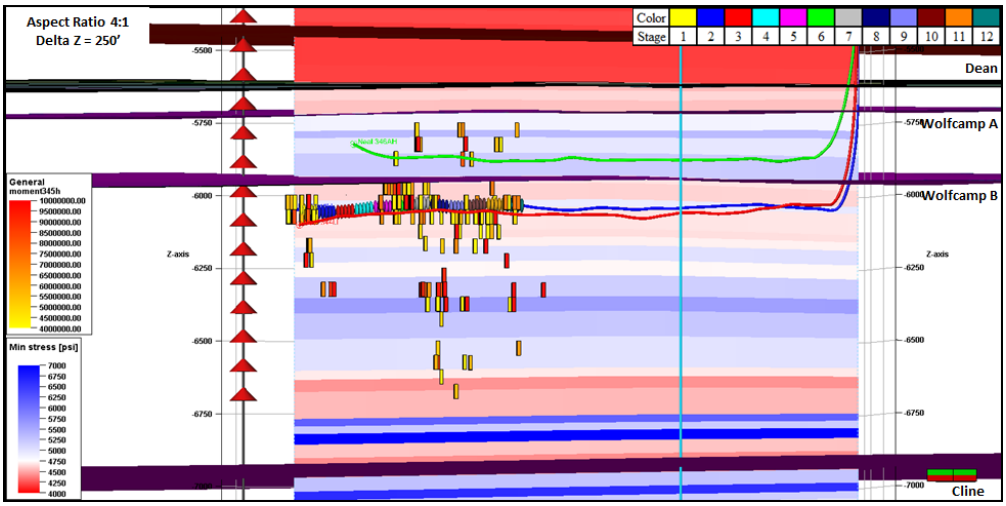

Figure 16: Depth view cumulative moment for the Neal 345H well, summing the seismic moments of the microseismic events within 50' cell sizes. Seismic moments less than 4E+6 NM are filtered out. Coloring scale is from yellow to red corresponding to seismic moment of 4E+6 NM to 1E+7 NM

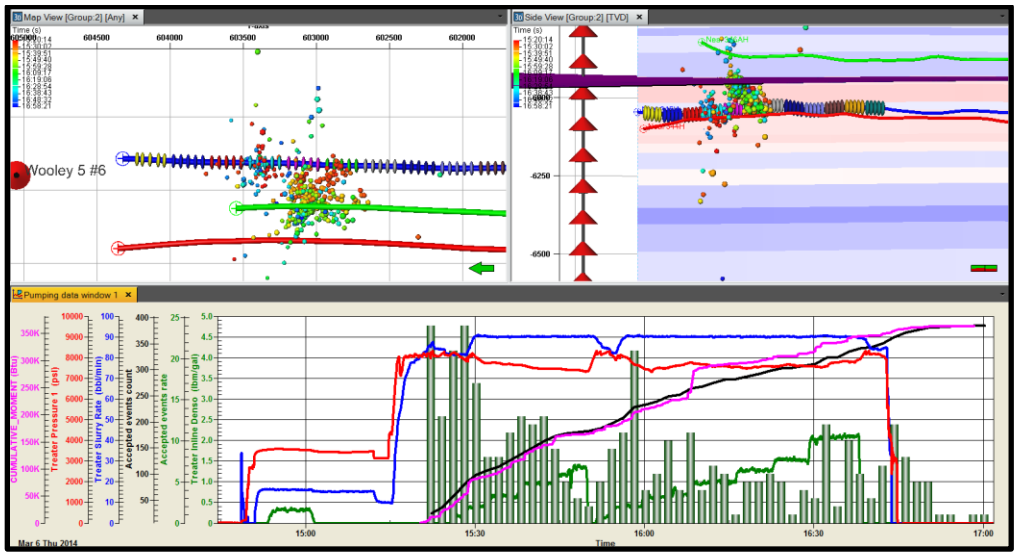

Figure 17: 345H Stage 5: Top left image showing microseismic events in map view colored by time and sized by magnitudes; Top right image showing microseismic events in depth view against zoned stress profile; Bottom graph showing Treatment Plot with Surface Pressure (red), Treatment Slurry Rate (blue), Proppant Concentration (green), MS event rate (bars), MS event count (purple) and MS cumulative moment (black curve)

On the other hand, the Neal 345H stage 10 stimulation sees the majority of the microseismic height growth (Figure 18) occurring downward into deeper portions of the formation. The bulk of the event density is again clustered within the lower stress zones of the Wolfcamp B formation that correspond to the lower stress zones located beneath the wellbore as opposed to above the wellbore, which was observed with the stage 5 stimulation. The time dependent difference in the propagation of the microseismic distribution could potentially be indicative of the changes in the formation properties that are essentially driving the distribution and potentially the fracture growth.

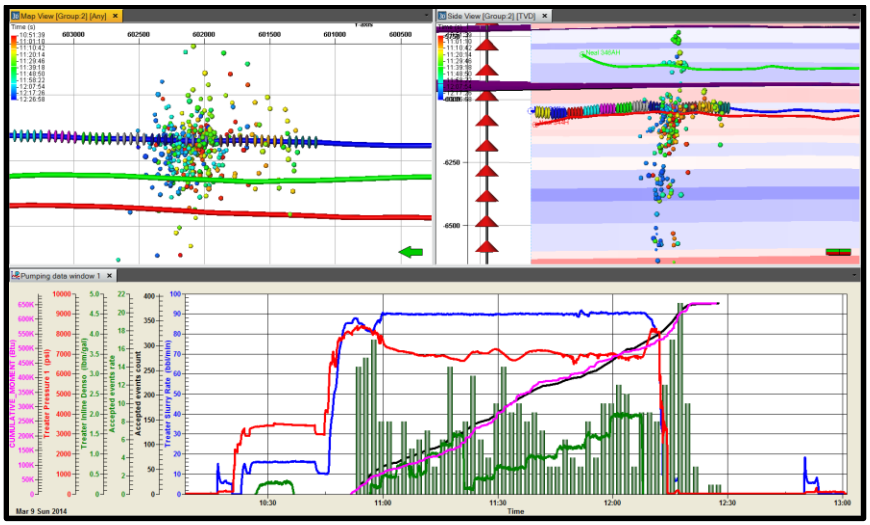

Figure 18: 345H Stage 10: Top left image showing microseismic events in map view colored by time and sized by magnitudes; Top right image showing microseismic events in depth view against zoned stress profile; Bottom graph showing Treatment Plot with Surface Pressure (red), Treatment Slurry Rate (blue), Proppant Concentration (green), MS event rate (bars), MS event count (purple) and MS cumulative moment (black curve)

Fracture Simulation Correlation with Microseismic Parameters

In an attempt to understand fracture geometry and its characterization from microseismic activity and extracted dimensions, a 3D fracturing simulation workflow (Planar3D) was performed. For consistency purposes, there were no step rate tests prior to the stimulation or any post frac production logs to help determine the number of clusters taking fluid. Therefore, all clusters are assumed to be active and taking fluid regarding the simulation results presented herein. Identical pumping schedule is also used for all the stages, as the actual executed pump schedule did not deviate significantly from the initial design.

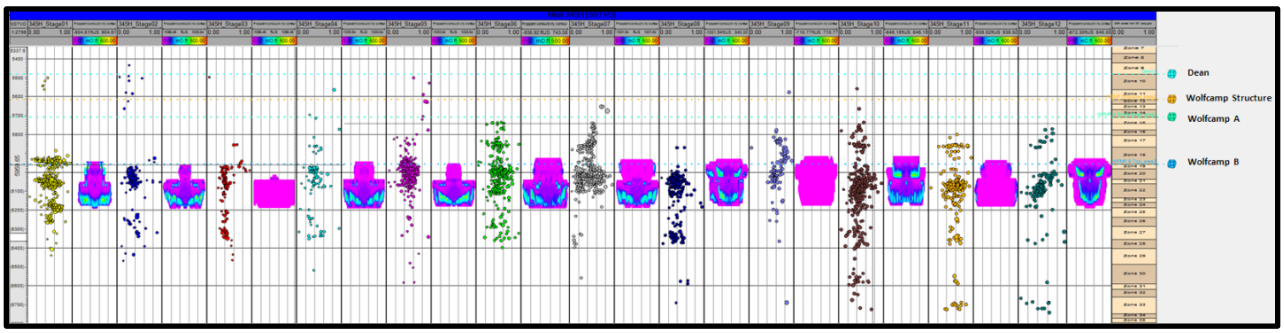

Figure 19: Neal 345H Stages 1 through 12 Microseismic Events and Frac Simulation Results respectively displayed in depth in chronologi cal order

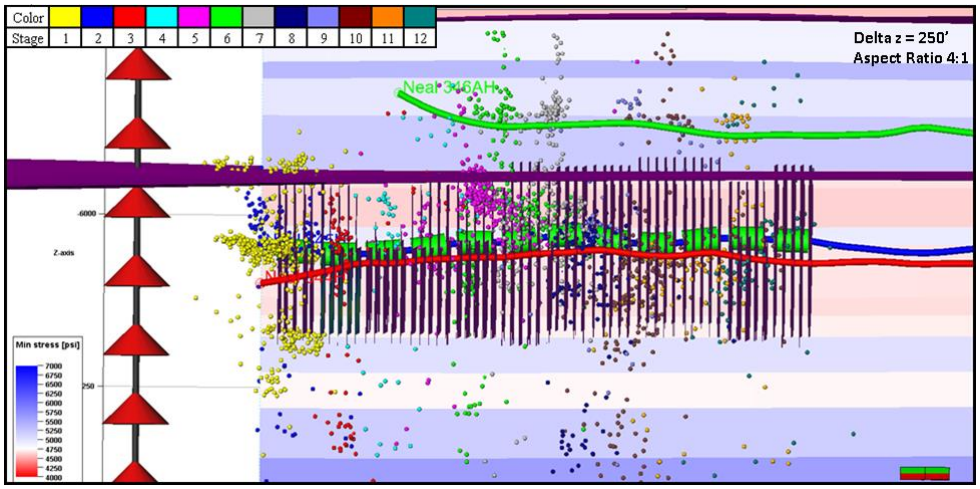

Figure 20: Side view displaying Neal 345H stages 1 through 12 Planar3D Frac Simulation results to represent the simulated height growth in relation to the stress barriers in the formation along with the microseismic events colored by stage

Simulation frac heights are relatively consistent for the majority of the stages. They also appear to be more confined than the microseismic results as expected. Toe-ward stages 1 through 3 and possibly 4, which are not aligned with stages from the shallower 346AH, tend to show greater similarities between the simulated and microseismic heights. The Wolfcamp A lateral appears to have obviously impacted the upward height growth developed. However, that observation does not apply to all the stages that show alignment across the 346AH and 345H laterals.
Figures 21 and 22 present numerical comparisons between simulated fracture heights and the measured microseismic heights that have been extracted using 3 different sets of outlier filters applied to the events.

345H Planar3D Frac Simulation Results													
Frac Simulation Results	STG1	STG2	STG3	STG4	STG5	STG6	STG7	STG8	STG9	STG10	STG11	STG12	Average
HF Width at well (inches)	0.14	0.13	0.14	0.13	0.13	0.13	0.16	0.13	0.14	0.15	0.13	0.14	0.14
HF Height at well (ft.)	267	243	269	258	250	280	253	246	255	256	269	246	258
Propped Width at well (inches)	0.14	0.13	0.14	0.13	0.13	0.13	0.15	0.13	0.14	0.15	0.13	0.13	0.14
Propped Height at well (ft.)	248	217	149	232	228	247	219	220	220	220	244	219	222
Av conductivity (md.ft.)	77	68	80	65	76	66	68	63	71	78	71	66	71
EOJ net pressure (psi)	115	119	136	14	-114	-158	-137	-43	-134	-110	-110	-70	-41

Figure 21: Neal 345H Frac Simulation Results: stages 1-12

	345H Microseismic Heights using 5%, 10% and 15% outlier filters								
	5% outlier filter			10% outlier filter			15% outlier filter		
	Downward MS Height	Upward MS Height	Total	Downward MS Height	Upward MS Height	Total	Downward MS Height	Upward MS Height	Total
STG1	213'	137'	349'	213'	137'	349'	155'	137'	292'
STG2	376'	557'	933'	331'	481'	812'	278'	88'	367'
STG3	303'	203'	506'	289'	89'	377'	289'	89'	377'
STG4	291'	334'	625'	291'	234'	525'	291'	187'	478'
STG5	439'	225'	664'	204'	214'	418'	062'	165'	227'
STG6	310'	303'	613'	310'	303'	613'	251'	303'	554'
STG7	309'	288'	597'	83'	278'	361'	075'	265'	340'
STG8	337'	165'	502'	322'	165'	487'	332'	165'	497'
STG9	217'	351'	568'	217'	226'	443'	155'	217'	372'
STG10	612'	282'	894'	546'	282'	828'	546'	282'	828'
STG11	692'	232'	924'	692'	179'	871'	692'	179'	871'
STG12	659'	239'	898'	659'	239'	898'	659'	201'	860'

Figure 22: Neal 345H Microseismic Heights using 5%, 10% and 15% outlier filters

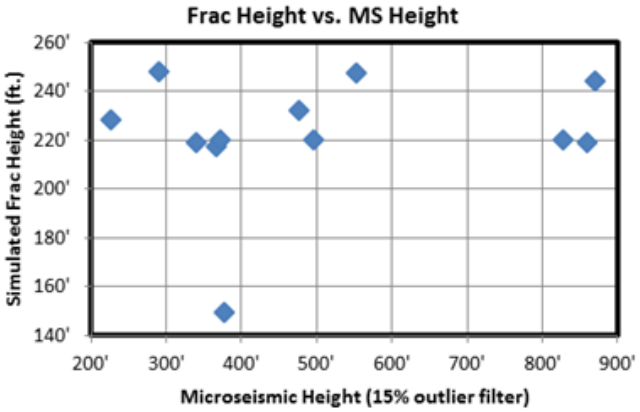

Figure 23: Simulated Frac Height vs. Microseismic Height extracted using a 15% outlier filter

Although there appears to be no clear correlation between the simulated fracture and microseismic heights (Figure 23), the fracture heights appear to be smaller and more confined than the microseismic growth. The variability in geometry however, continues to be unclear. To bring closure onto this challenge, seismic measurements are then integrated with the microseismic results.

Unlocking the Potential of 3D Surface Seismic Integration with Microseismic Measurements:

Figures 24 through 30 show arbitrary seismic cross sections length wise along lateral trajectories of the 345H and 344H wells with the microseismic (MS) data. When combining the formation properties obtained from the inverted seismic p-impedance, the delineation of lateral changes along wellbores and at different depths becomes essential when correlating variations seen in microseismic response and subsequent changes in hydraulic fracture geometry developed. These parameters extrapolated from seismic can be used on a stage by stage basis which was shown in Figure 9. For example, a twofold criterion can be used when interpreting mineralogical and geomechanical data from the surface seismic integrated with observed fracture propagation behavior inferred from MS events. Incidentally, this could also be used as a means to high grade acreage for development.

The first criteria is the delineation of an ideal mechanical bench for landing that has higher impedance, and is thus characteristic of high volume of calcite and Young's Modulus for enhanced brittleness. This would result in efficient hydraulic fracture initiation of wide fracture networks nearest the wellbore to allow for optimal slurry rates to be pumped, and for the embedment of proppant into the shallower flooding surface above. The second criteria would be for fracture containment in areas of greater ductility. This would include those areas that map flooding surfaces with significantly lower values of p-impedance for increased volume of clay (and perhaps kerogen). Fracture containment becomes increasingly critical when operators implement "chevron-type patterns" for stacked horizontal wells that are vertically spaced at minimal distances, and would potentially prevent the fracturing and thieving of oil production from adjacent pay zones.

For example, Figure 24 shows a p-impedance seismic cross section with the microseismic events representing the 345H. Investigating the first criteria shows a high density of MS events in stages 5 through 10 where the well was landed in an area of higher impedance (or blue color). For criteria two, the seismic event (or flooding surface) above the landing bench is representative of particularly lower impedance between stages 5 through 10, and may be acting as a ductile barrier to contain fracture propagation to within the zone. Notice that the MS heights at these stages are minimal and appear not to extend into the zone above which represents the Wolfcamp A resource which the 346AH is producing from. Individual stages have also been highlighted in Figure 25. Particularly, notice stage 5 MS events which show greater heights, perhaps due to a less ductile overlying flooding surface at this location.

Also, stage 5 MS events show an unusual geometry and subsequent fracture pattern, and potentially demonstrate the propagating "front" of fractures aligning horizontally along the base of the flooding surface (and perhaps along natural fractures) then propagating up into the zone above as stress levels permit. The stage 5 unique behavior of MS events can also be interpreted from the flooding surface map shown in Figure 26 (right panel) where stage 5 pink events appear to propagate away from lower impedance, or areas of higher ductility and less brittleness. Likewise, the 344H well, also landed in the Wolfcamp B bench, is shown in Figure 28 with stages 4-7 highlighted in Figure 29. Again, the MS events appear to propagate away from areas of greater ductility, until higher brittleness is encountered at which point fracture heights appear to significantly increase where a high number of MS events are recorded within the Wolfcamp A bench.

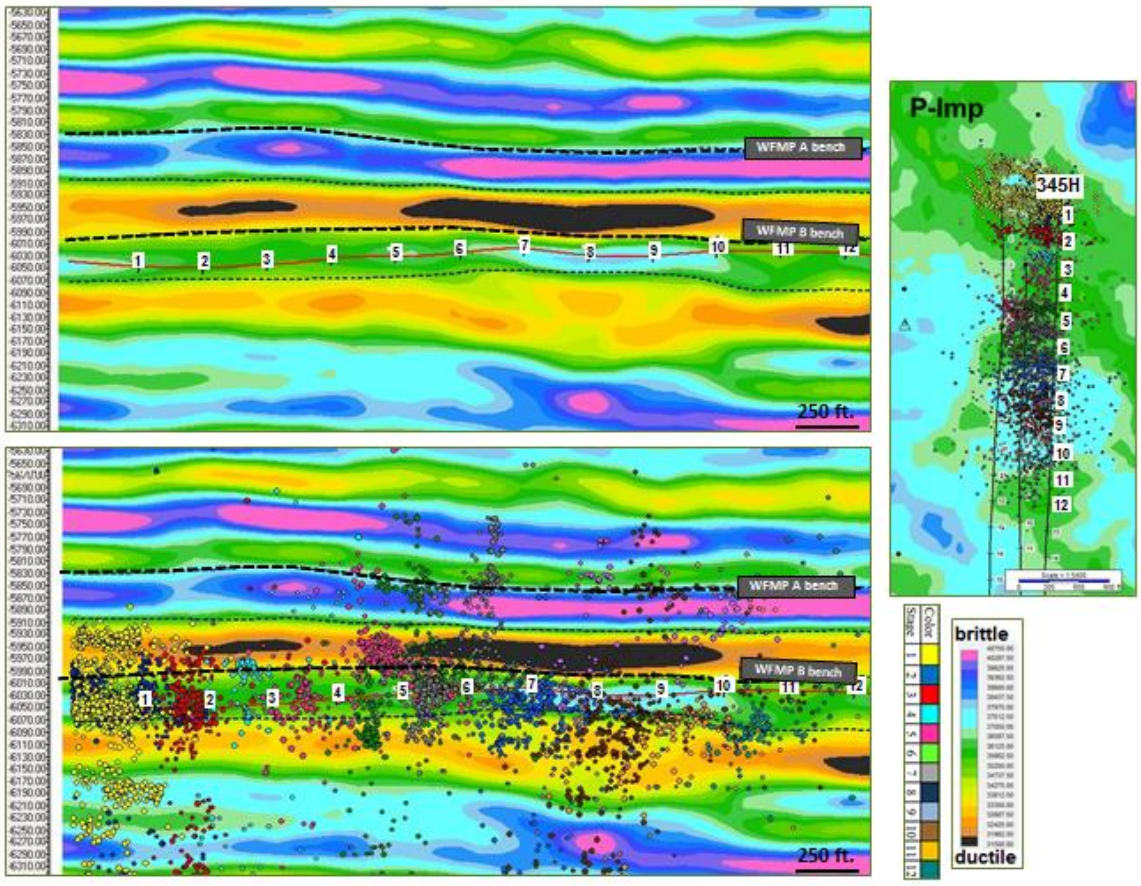

Figure 24: Well 345H microseismic data with seismic impedance cross sections.

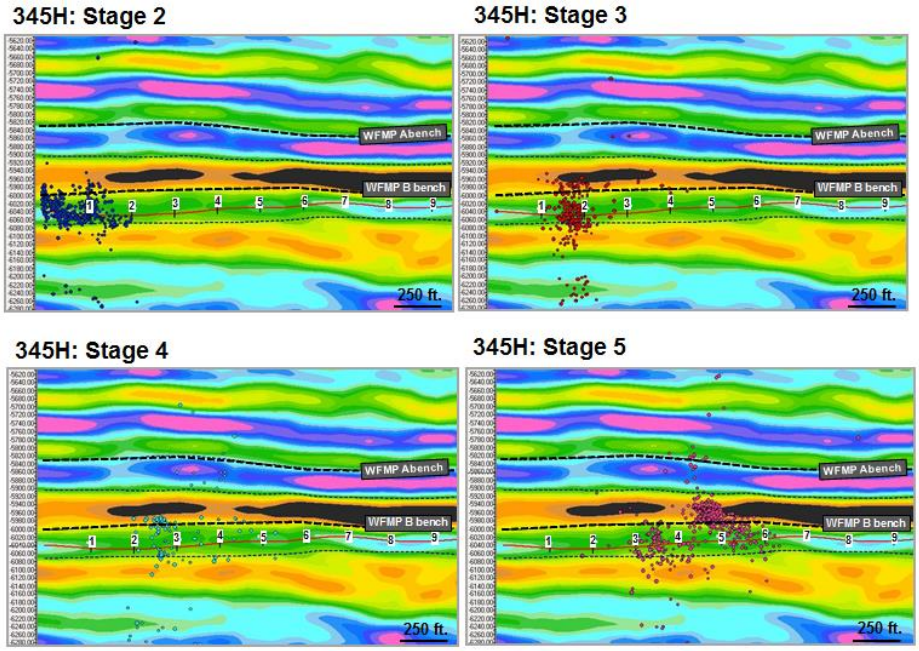

Figure 25: Well 345H microseismic data (stages 2-5) with seismic impedance cross sections.

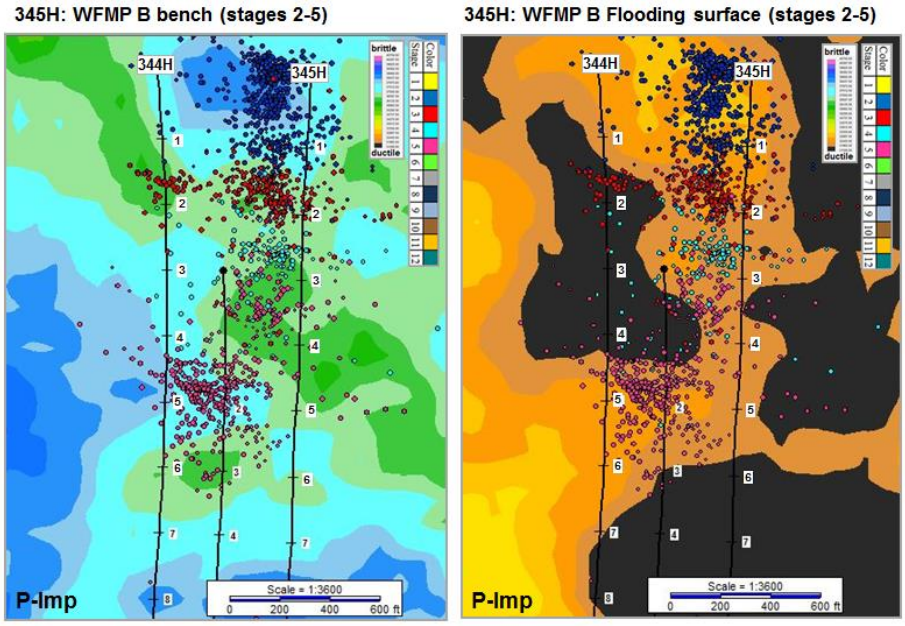

Figure 26: Well 345H microseismic data (stages 2-5) with P-Imp maps of the Wolfcamp B bench and flooding surface.

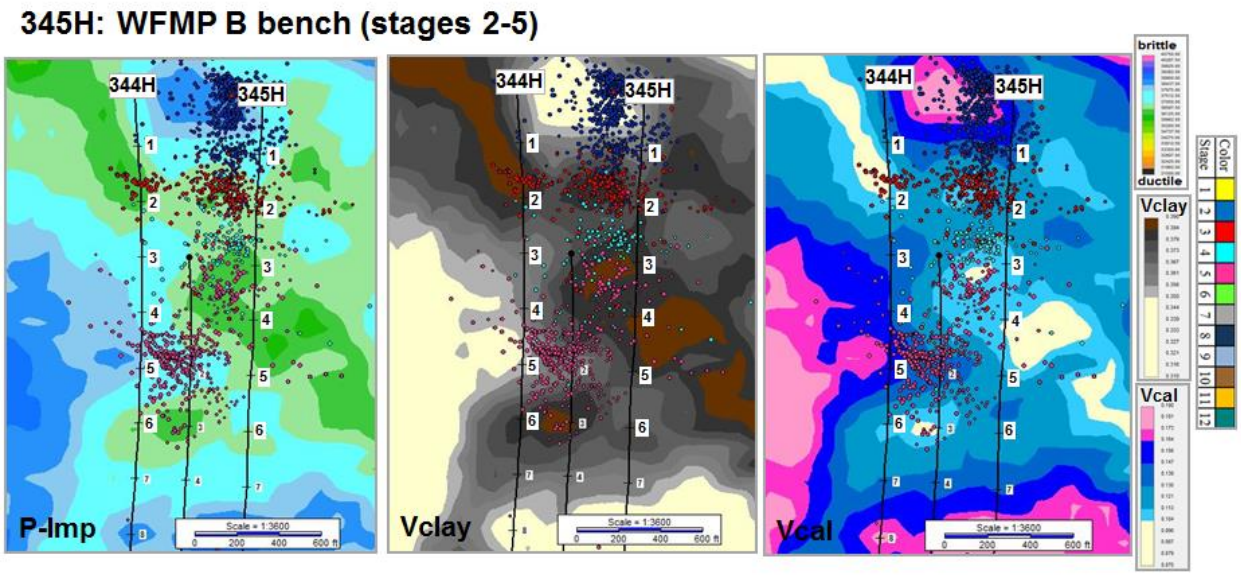

Figure 27: Well 345H microseismic data (stages 2-5) with maps showing Wolfcamp B bench P-Imp, Vclay, and Vcal.

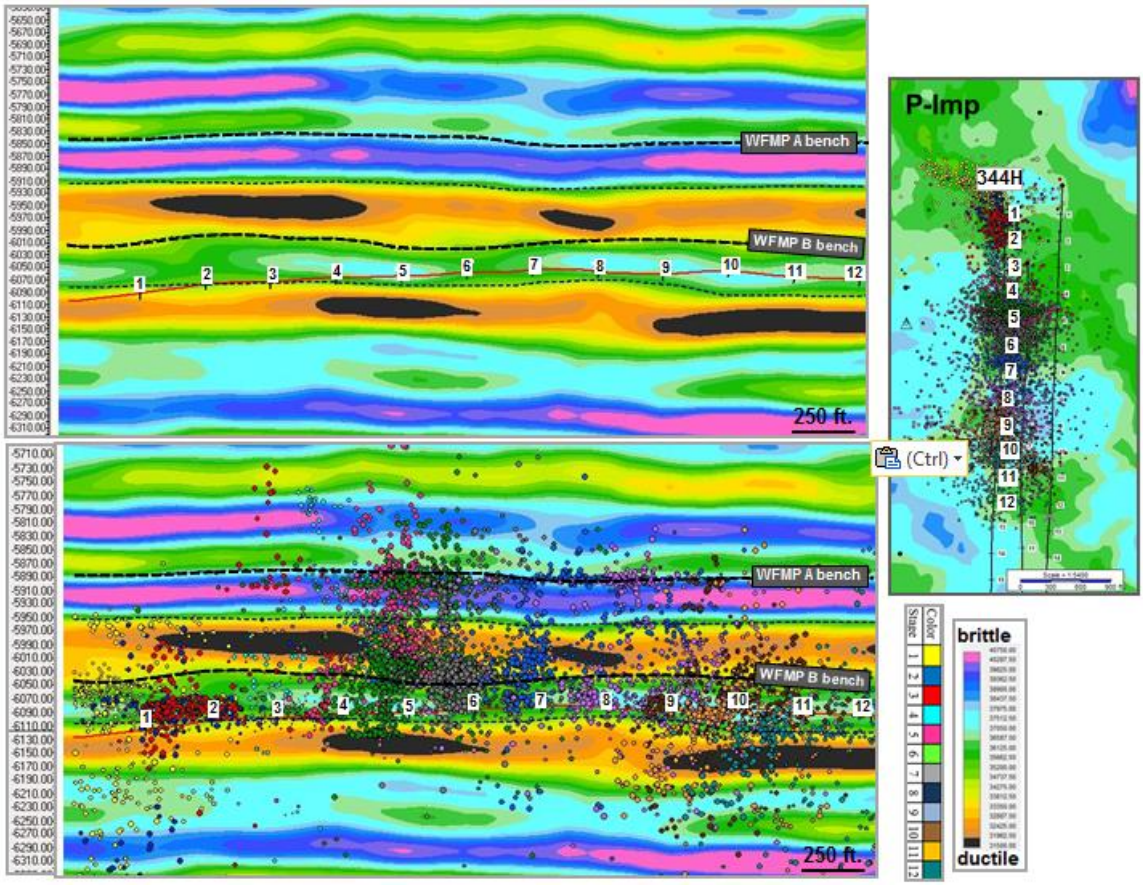

Figure 28: Well 344H microseismic data with seismic impedance cross section.

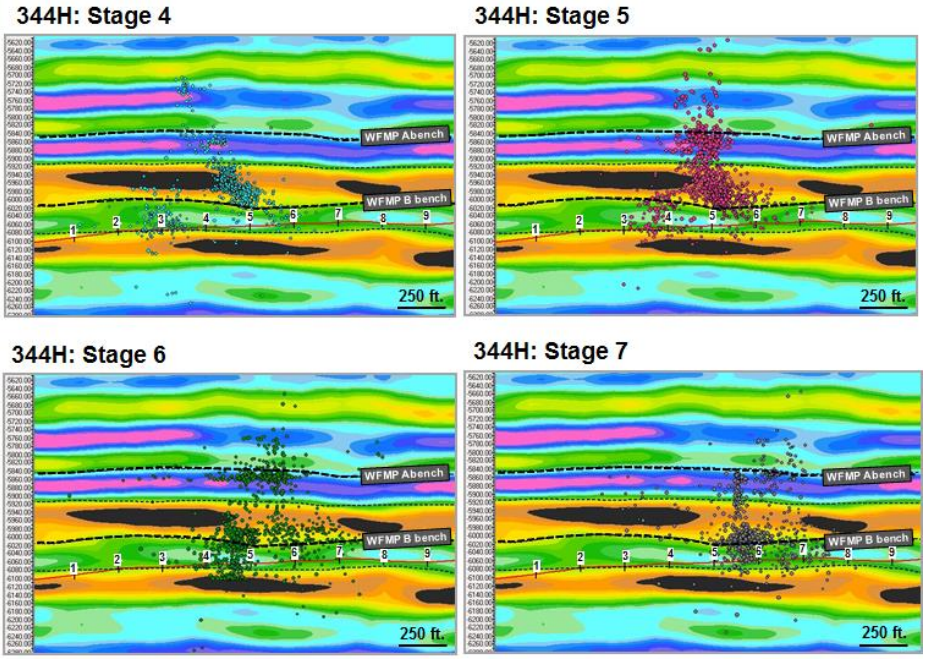

Figure 29: Well 344H microseismic data (stages 4-7) with seismic impedance cross sections.

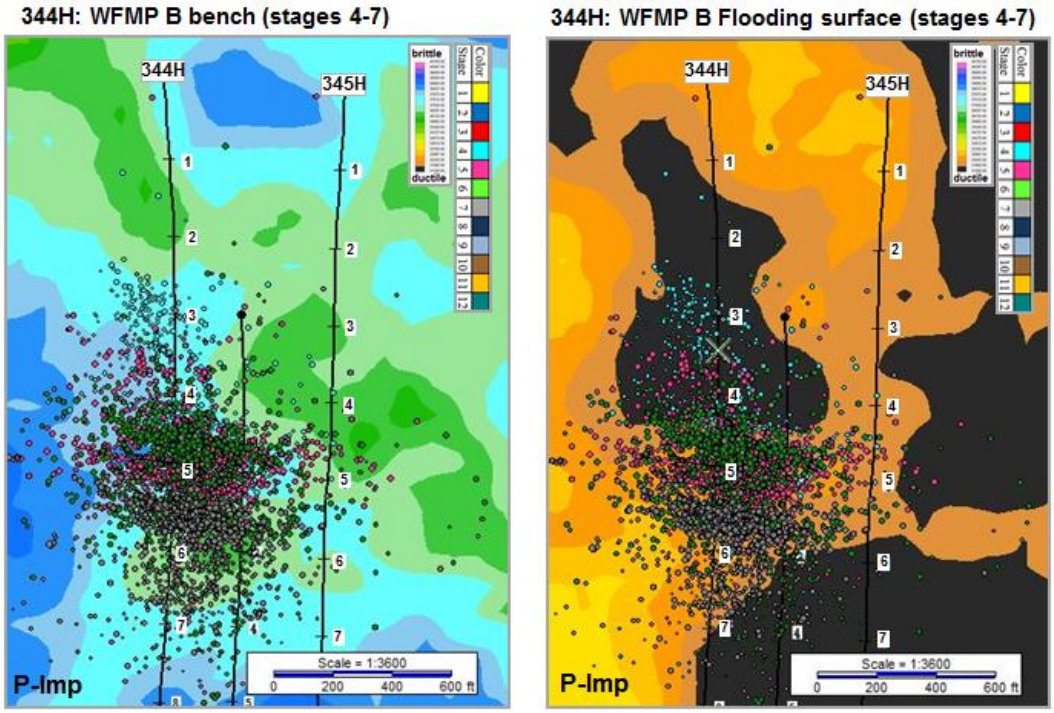

Figure 30: Well 344H microseismic data (stages 4-7) with P-Imp maps of the Wolfcamp B bench and flooding surface.

Conclusions

It was shown that a high degree of vertical and lateral heterogeneity exists within the Wolfcamp formation that is geology driven, and results from the irregular stacking of discrete depositional carbonate units resulting in varying mineralogy compositions that ultimately define and correlate with geomechanical properties characterized by relative fracability and brittleness. These mechanical properties ultimately influence resultant fracture stimulation geometries including prop height and half-length which in turn require calibration to microseismic and completions data. This empirical approach demonstrates the integration of said multidisciplinary measurements to optimize completion parameters with lower costs in implementing a "smart frac" –type stage by stage analysis, and to improve fracture modeling workflows using rock properties from seismic nearest the wellbores for a more complete and accurate solution ultimately resulting in optimal production rates.

References

Hobson, J. P., Caldwell, C. D., and Toomey, D. F., 1985a, Early Permian deep-water allochthonous limestone facies and reservoir, west Texas: American Association of Petroleum Geologists Bulletin, v. 69, p. 2130–2147.

Mazzullo, S. J., and Reid, A. M., 1987, Basinal Lower Permian facies, Permian Basin: part II—depositional setting and reservoir facies of Wolfcampian–lower Leonardian basinal carbonates: West Texas Geological Society Bulletin, v. 26, no. 8, p. 5–10.

N. Zakhour, M. Sunwall, R. Benavidez, L. Hogarth, J. Xu, 2015. Real-Time Use of Microseismic Monitoring for Horizontal Completion Optimization Across a Major Fault in the Eagle Ford Formation, Paper SPE 173353-MS

Rickman, R., Mullen, M. J., Petre, J. E., Grieser, W. V., & Kundert, D. (2008, January 1). A Practical Use of Shale Petrophysics for Stimulation Design Optimization: All Shale Plays Are Not Clones of the Barnett Shale. Society of Petroleum Engineers. doi:10.2118/115258-MS

Saroka, W. L., and M. L. Shoemaker, 2003, Impedance inversion in a structurally complex carbonate environment: 73rd Annual International Meeting, SEG, Expanded Abstracts, 398–401

Shoemaker, M.L., Hill, W.A., and Trumbly, P.T, 2006 Implications of wavelet analysis to reservoir quality and reserve estimation: A systematic approach to wavelet estimation with an example case study from the deep Tuscaloosa Trend, Pointe Coupe Parish, Louisiana, USA. SEG Technical Program Expanded Abstracts 2006: pp. 1103-1107.

Silver, B. A., and Todd, R. G., 1969, Permian cyclic strata, northern Midland and Delaware Basins, West Texas and southeastern New Mexico: American Association of Petroleum Geologists Bulletin, v. 53, p. 2223–2251

Wilson, J. L., 1975, Carbonate facies in geologic history: New York, Springer-Verlag, 471 p.

X. Yu, J. Rutledge, S. Leaney, S. Maxwell, 2014. Discrete Fracture Network Generation from Microseismic Data using Moment-Tensor Constrained Hough Transforms, Paper SPE-168582-PT